Sensorless adaptive optics multimodal en-face small animal retinal imaging

DANIEL J. WAHL,[1] RINGO NG,[1] MYEONG JIN JU,[1] YIFAN JIAN,[1,2] AND MARINKO V. SARUNIC[1,*]

[1]*Engineering Science, Simon Fraser University, Burnaby, BC, Canada*
[2]*Casey Eye Institute, Oregon Health & Science University, Portland, OR, USA*
[*]*msarunic@sfu.ca*

Abstract: Vision researchers often use small animals due to the availability of many transgenic strains that model human diseases or express biomarkers. Adaptive optics (AO) enables non-invasive single-cell imaging in a living animal but often results in high system complexity. Sensorless AO (SAO) can provide depth-resolved aberration correction with low system complexity. We present a multi-modal sensorless AO *en face* retina imaging system that includes optical coherence tomography (OCT), OCT-angiography, confocal scanning laser ophthalmoscopy (SLO), and fluorescence detection. We present a compact lens-based imaging system design that allows for a 50-degree maximum field of view (FOV), which can be reduced to the region of interest to perform SAO with the modality of choice. The system performance was demonstrated on wild type mice (C57BL/6J), and transgenic mice with GFP labeled cells. SAO SLO was used for imaging microglia (Cx3cr1-GFP) over ~1 hour, where dynamics of the microglia branches were clearly observed. Our results also include volumetric cellular imaging of microglia throughout the inner retina.

1. Introduction

The study of small animal models of human diseases causing blindness is important to understand the mechanisms of vision loss and to develop novel therapies. Conventional histological approaches require sacrificing the animal at each study time point. Non-invasive imaging is highly desirable for longitudinal studies, reducing the effects of inter-animal variation and reducing the number of animals required for a study. There would be potential benefits and advancements if more researchers had access to high resolution *in vivo* imaging systems with the functional and structural detection capabilities that were previously only attainable through histology [1]. Furthermore, *in vivo* imaging allows for the study of physiological processes such as the dynamics of microglia [2,3].

Theoretically, the Numerical Aperture (NA) through the pupil of the mouse eye permits sub-micrometer imaging of the retina. However, optical aberrations introduced by the tear film, cornea, and intraocular lens reduce the actual resolution. In order to approach diffraction limited imaging, these aberrations can be corrected with Adaptive Optics (AO) using a wavefront corrector such as a Deformable Mirror (DM) [4,5].

AO has been implemented in many ophthalmic imaging modalities such as Optical Coherence Tomography (OCT), Scanning Laser Ophthalmoscopy (SLO), and fundus photography, which have been well documented in References [1,5–10]. The traditional approach to AO is to use a Wavefront Sensor (WFS) to measure the ocular aberrations directly. For example, AO SLO has been demonstrated for *in vivo* imaging with cellular resolution of Green Fluorescent Protein (GFP) labeled cells [5,11,12]. Performing accurate wavefront measurements for WFS AO imaging in a small animal retina, requires a high level of system complexity due to the short length of the eye creating an optically thick sample with multiple scattering surfaces [4]. Alternatively, Sensorless AO (SAO) has the potential to allow for systems to be compact, easily operated, robust, and inexpensive. SAO does not

require direct measurements of the optical wavefront but instead uses an image-based aberration correction approach, such as a multi-dimensional optimization or pupil segmentation [13,14]. SAO methods have the ability to provide depth resolved aberration correction by using images acquired at specific layers within the retina. For example, AO OCT has been demonstrated using *en face* projections extracted from three dimensional OCT volumes to drive the optimization algorithm on the selected retinal layers [15].

The multi-modal system in this report was designed to incorporate SAO with multiple modalities including Optical Coherence Tomography (OCT), OCT based Angiography (OCT-A), confocal Scanning Laser Ophthalmoscopy (SLO), and fluorescence detection. In this work, we present a compact lens-based design of a imaging system for multi-purpose imaging of the small animal retina, which has significantly improved performance and functionality since previous reports [15–18]. The *en face* and cross-sectional imaging enable visualization of the retinal structure while the fluorescence imaging has the ability to visualize the biological function of the retina through labeled reporter cells. OCT and SLO can be combined to employ a multi-modal system for simultaneous and co-localized structural and functional imaging. We present representative images and analyses to demonstrate the performance, versatility, and usability of the system for small animal imaging. Images acquired prior to SAO aberration correction demonstrate the widefield and standard resolution imaging in a mouse eye. After performing SAO optimization, our results demonstrate high resolution imaging featuring *in vivo* volumetric and time-lapse imaging of fluorescently labeled microglia.

2. Methods

2.1 Optical design

A schematic of the optical layout of the system is presented in Fig. 1(a). The system components were assembled with off-the-shelf optomechanics and custom mounts designed with SolidWorks (Dassault Systèmes, France) as shown in the Fig. 1(b). The light sources for the imaging system included a near infrared (NIR) Superluminescent Diode (SLD, BLM2-D, Superlum Diodes Ltd., Ireland) for OCT using a central wavelength of 840 nm with a spectral bandwidth of ~80 nm, and a 488 nm laser (0488L-13A, Integrated Optics, Lithuania) for confocal SLO and fluorescence excitation.

The OCT subsystem was based on a fiber optic Michelson interferometer. The OCT light was split by a 70:30 single mode optical fiber coupler (AC Photonics Inc, CA, USA). The 70% portion of the light was connected to a reference arm consisting of a fiber collimator, a dispersion compensation block and a mirror. The OCT probe beam was the 30% portion of light from the coupler, which was launched from a reflective collimator (RC04FC-F01, Thorlabs Inc., NJ, USA) and transmitted through a cold mirror (ZT670rdc-xxrxt, Chroma Technology Corp, VT, USA) for combination with the 488 nm SLO light.

In the SLO subsystem, another reflective collimator (RC08FC-F01, Thorlabs Inc., NJ, USA) was used to launch the SLO light from a fiber with a polarization controller, such that the horizontally polarized light was reflected from a Polarization Beam Splitter (PBS, PBS251, Thorlabs Inc., NJ, USA). The light was then reflected from a dichroic mirror (ZT405/488/561rpc-UF1, Chroma Technology Corp, VT, USA) to the cold mirror, and then co-aligned with the OCT light.

The first pupil plane of both subsystems was defined by the Variable Focus Lens (VFL, Arctic 39N0, Corning, NY, USA) with an aperture of 3.9 mm. The imaging beams were relayed and magnified to a continuous membrane DM (DM69, Alpao, France) with a 10.5 mm aperture, and then to a mounted pair of Galvanometer-scanning Mirrors (GM, 6210H, Cambridge Technology Inc., MA, USA) with a clear aperture of 3.0 mm. Finally, the light was reduced to a beam diameter of 1.0 mm to be focused by the mouse eye and relayed from the GM to be scanned across the retina with a maximum scanning angle of 50 degrees. The optical relays were constructed using achromatic doublets with an antireflection coating for

both visible and near infrared light (VIS-NIR Coated Achromatic Lenses, Edmund Optics). Each relay used two off-the-shelf lenses, except the final relay to the mouse eye. See L5 and L6 in Fig. 1. These elements were constructed from two achromatic lenses that were placed symmetrically with a <1 mm air gap [19, 20]. This design enabled shorter optical relay required for our desired scanning angles without introducing significant aberrations.
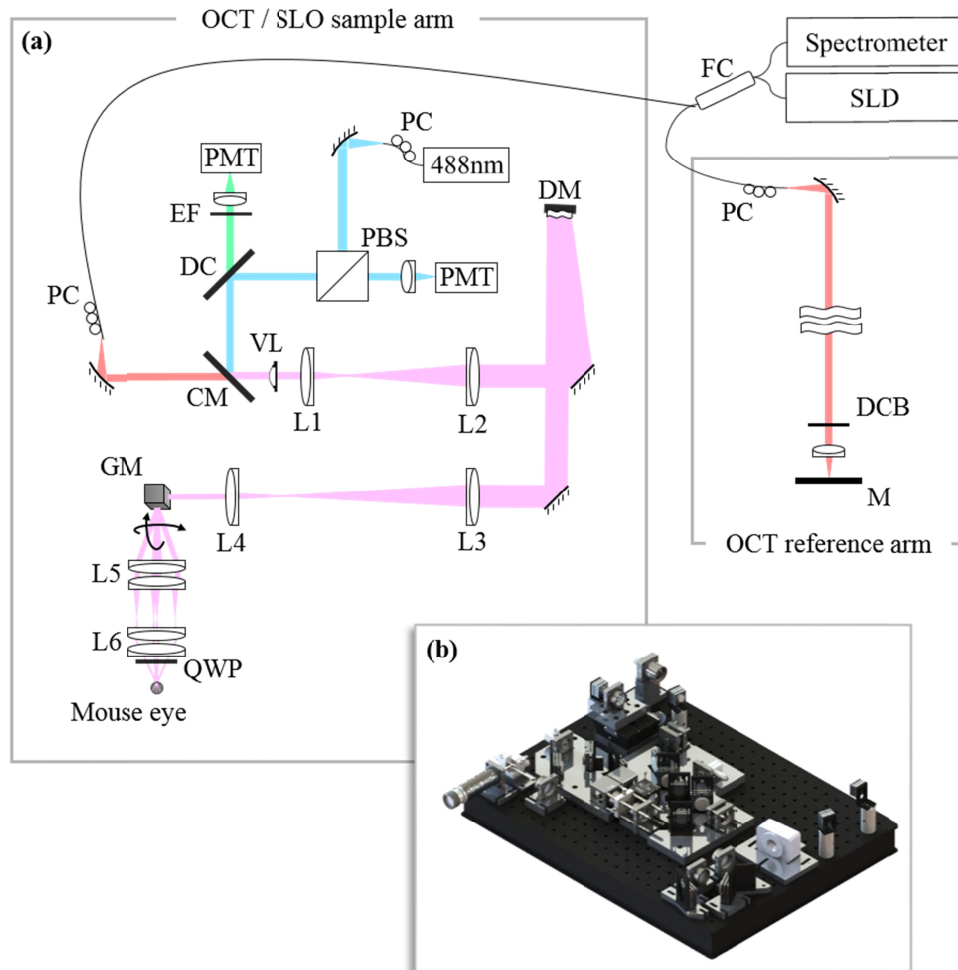

Fig. 1. (a) Schematic of Optical Coherence Tomography (OCT) and confocal Scanning Laser Ophthalmoscopy (SLO) system. The cyan represents the beam path of only 488 nm light, the green represents the beam path of only the fluorescence emission and the red represents the beam path of only the SLD light. The pink represents the co-aligned beam path of the 488 nm light, fluorescence emission, and SLD light. System components: Superluminescent diode (SLD), fiber coupler (FC), polarization controller (PC), polarization beam splitter (PBS), dichroic mirror (DC), emission filter (EF), cold mirror (CM), variable focus lens (VFL), deformable mirror (DM), galvanometer-scanning mirrors (GM), quarter wave plate (QWP), photomultiplier tube (PMT), dispersion compensation block (DCB), mirror (M). Achromatic doublet lenses: L1 = 50mm, L2 = 150mm, L3 = 300mm, L4 = 75mm, L5 = 2x125mm, L6 = 2x50mm. (b) Computer simulation of optical layout on custom optical mounts using OpticStudio and SolidWorks.

The final element before the mouse eye was a Quarter Wave Plate (QWP, WPQ10E-488, Thorlabs Inc., NJ, USA), which rotated the polarization state of the back-scattered SLO light from the sample so that the light would be transmitted by the PBS for detection [16,21]. Although this technique does not entirely remove the strongest reflection in the center of the

back-scattered SLO images (see the Results section), this method does remove other reflections from the optical elements. The optical design was simulated in OpticStudio (Zemax, WA, USA) and Fig. 2(a) presents the spot diagrams with an ideal model eye. The expected resolution and calculations were performed for mouse eyes using an NA of 0.25. The OCT and SLO spot diagrams are presented across a 15-degree (~500 µm for mouse eyes) Field of View (FOV) with 0 D of vergence at the sample pupil plane. The black circle in the top row represents the Airy disk with a ~2.1 µm radius for 820 nm, 840 nm, and 860 nm. The middle and bottom row have a 1.2 µm Airy disk radius for 488 nm SLO light. The bottom row represents the 488 nm spots scanned across 7 degrees (~230 µm for mouse eyes) with a 20 D vergence at the pupil plane for the eye produced by the simulated VFL. These FOVs (or smaller) are typically used for AO in the mouse eye [5], whereas for imaging a larger FOV, it may not be necessary to have a spot size on the order of microns. The axial resolution for OCT was estimated to be ~3 µm. For the SLO depth of focus, the non-confocal axial point spread function had a half width of ~21 µm. For the OCT-A imaging, the system was reconfigured to have a smaller beam into the eye, which reduced the NA to 0.15 and the Airy disk radius to 3.5 µm.

In order to reduce the overall size and simplicity of the system, we did not use an optical relay between the fast and slow scanning mirrors, which prohibited perfect conjugation to the pupil of the mouse eye with both scan axes. In Fig. 2(b), the amount of pupil wander in the mouse eye was simulated for the FOVs that are suitable for diffraction limited imaging.
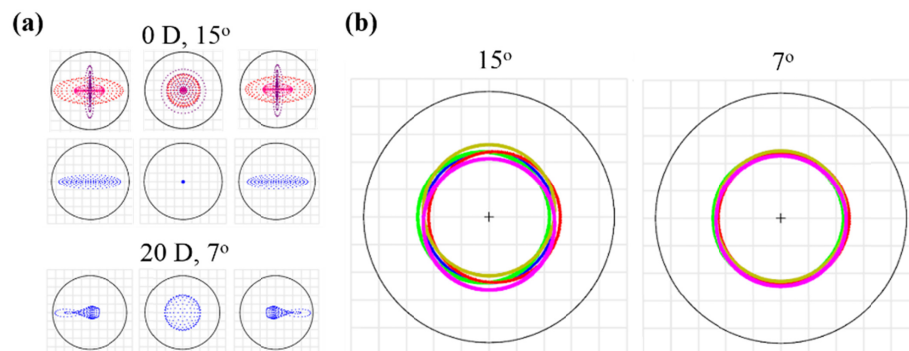

Fig. 2. (a) Spot diagrams of the OCT light at 820 nm (red), 840 nm (pink) and 860 nm (purple) across a 15-degree FOV, where the black circle represents the Airy disk with a 2.1 µm radius. Spot diagrams of the 488 nm (blue) SLO light scanned across a 15-degree FOV with 0 D of vergence at the sample pupil plane and 7-degress with 20 D of vergence at the sample pupil plane where the black circle represents the Airy disk with a 1.2 µm radius. (b) The boundary of the imaging beam at the final pupil plane of the system. The black circle represents a 2 mm aperture. Each color represents a different scan position across a 15-degree and 7-degree FOV to simulate the pupil wander due to the space between the scanning mirrors in the optical design.

The back-scattered OCT light from the sample was recombined with the reference arm light at the fiber coupler and directed to a spectrometer (Cobra 800, Wasatch Photonics, NC, USA). The A-scans were acquired with a frame grabber (PCIe-1433, National Instrument, Austin, TX) at 100 kHz and the OCT volumes were sampled at 1024 x 400 x 200 points. For OCT-A, two B-scans were acquired at the same location in the slow scan direction to calculate changes due to blood flow. The OCT/OCT-A cross-section and *en face* view were processed for real-time display using our custom GPU accelerated acquisition software [17,18,22] written in C/C + + .

The fluorescence emission was transmitted through the dichroic mirror, and the emission filter (ZET405/488/561m-TRF, Chroma Technology Corp, VT, USA), and then focused into a multimode fiber with a core diameter of ~2 Airy disk diameters (ADD) that directed the light to a photo-multiplier tube (PMT, H10723-20, Hamamatsu Photonics K. K., Japan). The

back-scattered 488 nm laser light was reflected from the dichroic mirror, transmitted through the PBS, focused into a multimode fiber with a core diameter ~5 ADD or ~20 ADD, and detected by another PMT (H7827-002, Hamamatsu Photonics K. K., Japan). We used a 5 ADD fiber core when performing image-based SAO with the back-scattered images, or else we used a 20 ADD fiber core, which provided the higher SNR for general navigation on the mouse retina. The PMT signal gain could be adjusted on the power supply depending on the amount of signal from the sample. The digitization (PCIe-6361, National Instrument, Austin, TX) of the PMTs was synchronized to the acquisition of the OCT A-scans for simultaneous imaging, otherwise the SLO could be operated alone at a 2 kHz line rate with a sampling density of 400 x 200 points.

2.2 Sensorless adaptive optics

The SAO could be performed on the *en face* projection of the OCT volumes, the back-scattered confocal SLO, or the fluorescence SLO images. We implemented a hill climbing Coordinate Search (CS) algorithm similar to our previous work [16,23], which provided an exhaustive search to find the optimal Zernike coefficients. The merit function for optimization was determined by the highest image sharpness (S_{img}) [24,25], defined by the sum of the intensity squared of each image pixel I(x,y) in Eq. (1).

$$S_{img} = \sum_{x,y} \left[I(x,y) \right]^2. \tag{1}$$

The CS algorithm started with a flat wavefront with an RMS ~0.05 μm, which was calibrated using a SH-WFS in the location of the GM scanners. Then, for the first mode (k) in a sequence, a range of coefficients ($\pm \alpha$) was applied to the DM. The coefficient (a_n^*) that corresponded to highest metric value was applied to the DM and the algorithm moved onto the next mode. For the first iteration, the sequence of modes began with a defocus ($k = 4$) value, then the astigmatisms, and continuing in ascending order up to the 21st mode for a total of 18 modes. The Zernike polynomials were ordered and reported using the mode number according to the OSA/ANSI standard [26]. The sequence of 18 modes was usually repeated for multiple iterations, typically 2 or 3 times, until the metric value no longer increased. Successive iterations would search coefficients ranges ($\pm \beta$) around the previously selected coefficients. Between iterations, the imaging FOV or location could be adjusted, as the features of interest became visible.

For high resolution imaging, SAO could be used to correct wavefront aberrations from the mouse eye using the output from of the different imaging modalities for the image-based optimization. During optimization, the sampling density of the OCT was decreased to 1024 x 400 x 20 which resulted in 19 seconds for each iteration of the optimization. When the SLO was used for optimization, the sampling was set to 400 x 100 and each iteration took a total of 12 seconds.

2.3 Animal handling

The animal imaging sessions were performed under protocols compliant to the Canadian Council on Animal Care and the approval of the University Animal Care Committee at Simon Fraser University. The mice were anesthetized with a subcutaneous injection of ketamine (100 mg/kg of body weight) and dexmedetomidine (0.1 mg/kg of body weight). A drop of topical solution (Tropicamide, 1%) was applied to dilate the ocular pupils. A rigid 0-Diopter contact lens was placed on the animal eyes to prevent the cornea from dehydration and then the animal was aligned without any further contact to the imaging system [27]. For fluorescein angiography, the mice were subcutaneously injected with 100 μL of 100 mg/mL fluorescein. Mice were purchased from the Jackson Laboratory, including wild type strain

(C57BL/6J) and transgenic strain with Enhanced Green Fluorescent Protein (EGFP) labeled retinal ganglion cells (Tg(Thy1-EGFP)MJrs/J) and microglia (B6.129P-Cx3cr1[tm1Litt]/J).

For retinal imaging, the OCT imaging light was limited to 620 μW. The SLO imaging light did not exceed 230 μW in this report and was limited to 100 μW when operating simultaneously with the OCT.

2.4 Image processing

Images in this work were generated by standard post-processing techniques, including steps to register and align frames to a template for averaging, using a combination of Matlab (MathWorks Inc, MA, USA) and ImageJ (National Institutes of Health (NIH), MD, USA) toolkits. The number of volumes and frames that were saved could be easily changed in the acquisition software. For the images presented in this work, we used the following parameters: for OCT, we recorded 5 volumes per acquisition in 4 seconds; for OCT-A images, only one volume was recorded per acquisition in 1.6 seconds; and for SLO, we recorded 50 to 100 frames per acquisition in 5 to 10 seconds. The OCT B-scans were aligned with a vertical translation to remove axial motion of the animal. Most of the B-scans presented in this report were an average of 5 adjacent B-scans within one volume with an exception that is explained in the results section.

The *en face* OCT images were generated using a Maximum Intensity Projection (MIP) between two manually selected horizontal lines corresponding to depths in the retina. Then, the *en face* OCT projections and the SLO frames were processed with the following procedure: 1) The registration process was initialized by manually selecting a single frame as the template to align the other frames; 2) Each frame was globally translated horizontally and vertically to maximize the cross-correlation with the template; 3) The frames were broken up into horizontal strips and each strip was translated horizontally and vertically to maximize the cross-correlation with the template [28,29]; 4) The frames were non-rigidly aligned to the template with a sum of squared differences similarity metric along cubic B-splines using the Medical Image Registration Toolbox (MIRT) [30]; 5) After registration, the frames were averaged and the black and white thresholds were adjusted to enhance the image brightness and contrast for presentation. All the B-scans in this report are presented in a linear intensity scale; 6) The images were scaled so that the vertical and horizontal dimensions have the same scale.

SLO frames from the back-scattered and fluorescence channels were simultaneously acquired, which would allow for co-registration if the fluorescence signal was insufficient [31]. However, in this work, the fluorescence images had sufficient signal to use directly for registration.

3. Results

3.1 Imaging without adaptive optics

For imaging large retinal features, a widefield image is preferred and it may not be necessary to perform SAO. Figure 3(a) demonstrates a 50-degree OCT B-scan and a 44-degree *en face* projection of the Outer Plexiform Layer (OPL) of a wild type mouse retina. Unlike the other B-scan images in this report, in Fig. 3(a), the vertical scanning was disabled and 200 B-scans were acquired, aligned, and averaged. In Fig. 3(b) and (c), the sampling density is increased with a 22-degree FOV and the focus was shifted with the VFL from the OPL to the Nerve Fiber Layer (NFL). The B-scans and *en face* images were registered and averaged as described in the previous section. The location of the B-scan is indicated by the red dashed line.
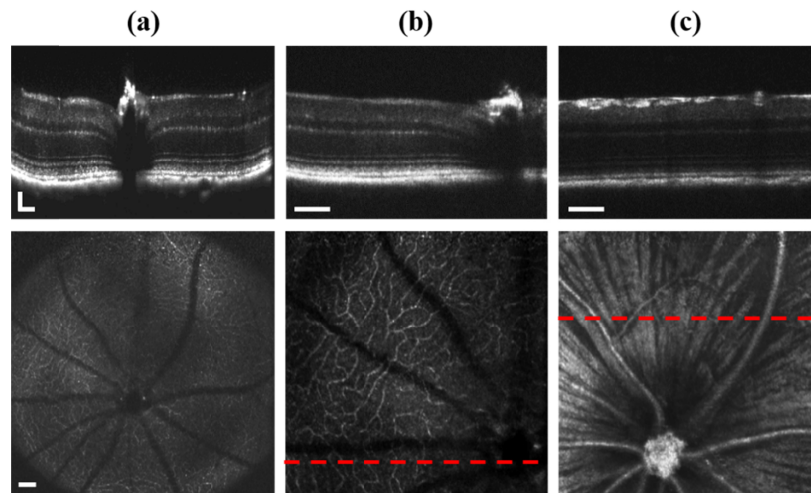
Fig. 3. (a) OCT B-scan across 50 degrees in the mouse retina and *en face* projection of the outer plexiform layer (OPL) across 44 degrees. The B-scan is an average of 200 consecutively acquired cross-sectional frames and the *en face* OCT image is an average of 5 frames. (b,c) Average of 5 adjacent OCT B-scans and an average of 5 *en face* OCT frames. The B-scans are located at the position of the red dashed lines. Vertical scale bar: 50 µm. Horizontal scale bars: 100 µm.

After acquiring OCT volumes, the OCT was disabled in the software so that the SLO could be operated at a faster speed. The structural SLO image in Fig. 4(a) was generated by the 488 nm back-scattered channel light from 50 averaged frames with the imaging light focused on the NFL and a 5 ADD confocal aperture. Fluorescence SLO images were generated from an average of 50 frames acquired a few minutes after a fluorescein injection. Images were acquired from three different vascular layers in the inner retina, including the NFL, inner plexiform layer (IPL), and OPL. These images were combined with a MIP for presentation in Fig. 4(b), which is demonstrated in further detail in the following results with AO.
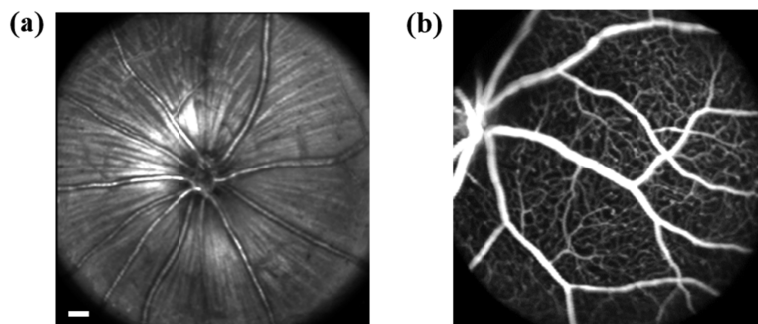

Fig. 4. Confocal SLO images of a mouse retina with 488 nm light. (a) Structural image of the nerve fiber layer from back-scattering. (b) Fluorescein angiography composited with a MIP from images of three different vascular layers. Scale bar: 100 µm.

OCT-A B-scans were created by calculating the difference between two intensity B-scans in the same location. Figure 5(a) shows the *en face* OCT-A image generated from the MIP of the OPL layer in the B-scans of a single volume. For comparison, Fig. 5(b) shows the *en face* OCT intensity image that was generated from the same OPL region. Figure 5(c) was created by coloring the *en face* OCT-A images that were extracted from the OPL with red, the IPL with green, and the NFL with blue.
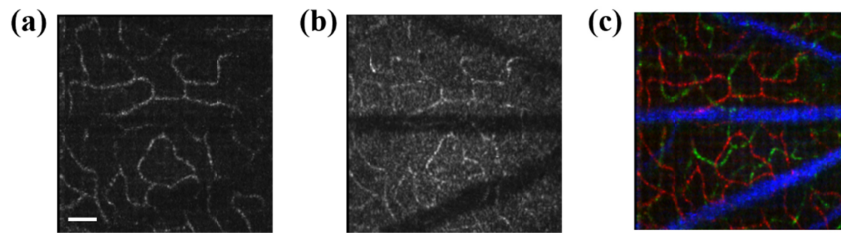
Fig. 5. (a) *En face* OCT-A images of the OPL in a mouse retina. (b) *En face* OCT intensity image from the same image data. (c) *En face* OCT-A images that were generated from the OPL (red), IPL (green), and NFL (blue). Scale bar: 50 μm.

3.2 Structural imaging with sensorless adaptive optics OCT and SLO

For SAO OCT, the retinal layer of interest was selected and the image quality metric was calculated on the *en face* image to drive the optimization. Figure 6 represents an example of an imaging sequence. The imaging plane was focused on the OPL layer with a FOV of ~250 μm. *En face* OCT images were used for optimization, and then OCT volumes were acquired for presentation. Figure 6(a) shows *en face* OCT images before and after SAO at different focal planes. Figure 6(b) demonstrates the two-iteration optimization with a plot of the image quality metric for each step in the optimization and the coefficients selected for each iteration. Overall, there was a 1.9-fold improvement in the image quality metric reported from the merit function of the optimization algorithm.
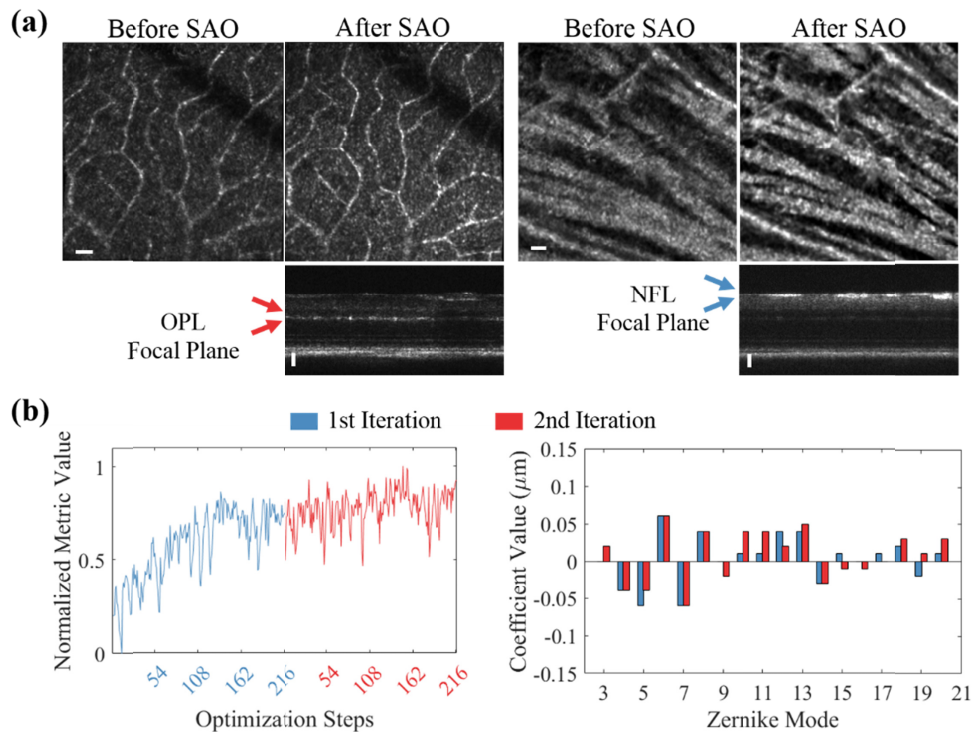

Fig. 6. (a) E*n face* images of the outer plexiform layer (OPL, top row, ~250 μm FOV) and nerve fiber layer (NFL, bottom row, ~280 μm FOV) retinal layers before and after Sensorless Adaptive Optics (SAO). SAO-OCT B-scans with the imaging focal plane on the OPL (red arrows) and NFL (blue arrows). (b) The normalized image quality for each step in the SAO optimization over two iterations and the Zernike coefficients selected for each iteration. Vertical scale bars: 50 μm. Horizontal scale bars: 20 μm.

Similarly, for SAO SLO, a typical imaging procedure is presented in Fig. 7. The confocal pinhole was 5 ADD for the structural SLO images in Fig. 7(a). In this case, the imaging light was focused on the NFL layer and the back-scattered SLO images were used for the optimization metric. Figure 7(a) shows the averaged SLO images before SAO and after SAO images of the NFL. Then the focus was shifted with the VFL to image different retinal layers including the OPL as shown. Figure 7(b) demonstrates the improvement in the image quality metric during the optimization. With a FOV of ~250 µm, the first iteration improved the image quality 2.2-fold. Then the FOV was reduced by half in the second iteration, which further improved the image quality 1.6-fold. The FOV could be changed for the successive iterations because new image quality values would be determined each iteration. Therefore, the plot of the image quality metric over the entire optimization had to be normalized independently for the metric values in each of these iterations. Figure 7(b) also presents the coefficients selected for each iteration.
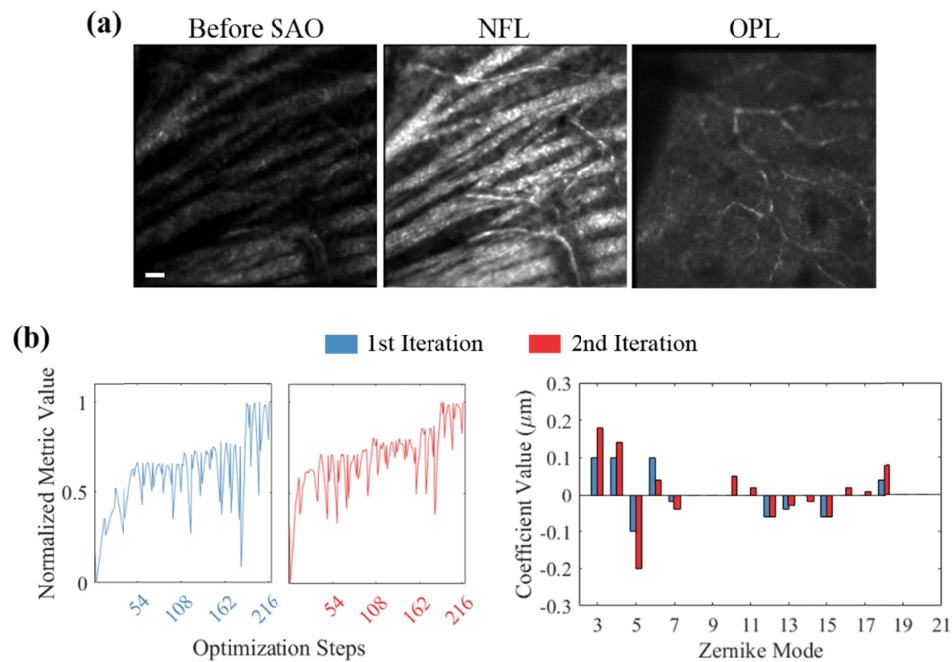

Fig. 7. (a) Confocal SLO images before and after Sensorless Adaptive Optics (SAO) of the nerve fiber layer (NFL) with a FOV ~250 µm. Images of the outer plexiform layer (OPL) after SAO. (b) The normalized image quality metric values for each step used for the SAO optimization for each iteration. The Zernike coefficients selected for each iteration. Scale bar: 20 µm.

For both SAO OCT (Fig. 6) and SAO SLO (Fig. 7), dark circular "holes" are revealed in between the nerve fiber bundles after aberration correction similar to other AO-SLO images [5], which are speculated to be retinal ganglion cell soma due to the size and shape.

3.3 Fluorescence imaging with sensorless adaptive optics

The ability to image EGFP labeled cells with the SAO SLO fluorescence detection further increases the functionality of the imaging system. The results in this section demonstrate the SAO SLO image quality and the abilities of the fluorescence detection channel. The structural confocal SLO images in this section were acquired with the detection pinhole ~20 ADD.

For Fig. 8, a larger FOV (~750 µm) was used to locate the EGFP labeled Retinal Ganglion Cell (RGC). The imaging FOV was reduced to ~250 µm to perform SAO on the fluorescence imaging channel, then a second iteration was performed on a further smaller FOV ~100 µm

with only dendrites of the RGCs in view. Figure 8(a) presents a comparison of the images acquired before and after SAO, including a line plot across between the blue (before SAO) and red arrows (after SAO). Figure 8(b) presents the structural images that were acquired when the imaging plane was focused on the RGC axon. In the right column, the structural image was colored in magenta and the fluorescence image was overlaid in green in order to better localize the RGC.
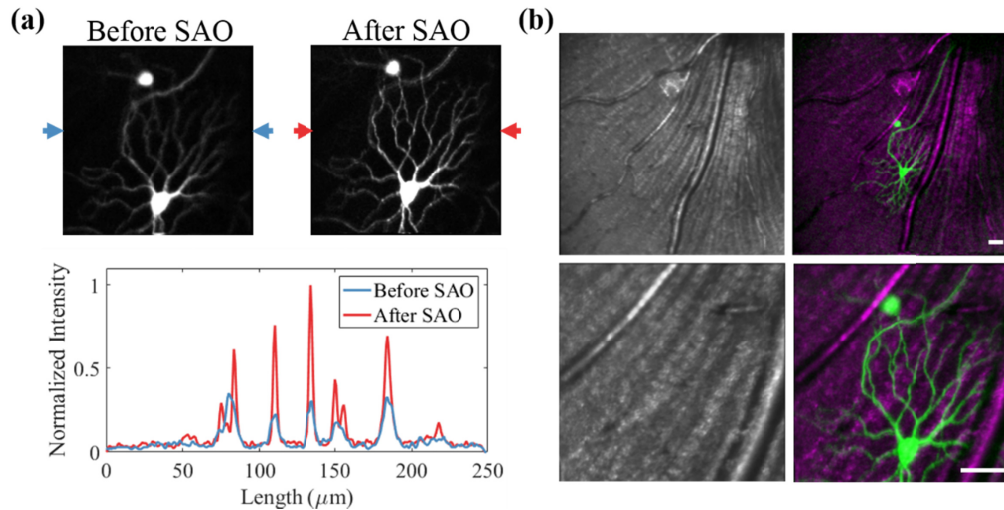

Fig. 8. Confocal SLO images of a mouse retina with labelled retinal ganglion cells (Tg(Thy1-EGFP)MJrs/J). (a) Fluorescence images before and after Sensorless Adaptive Optics (SAO) and an intensity line plot between the blue arrows (before SAO) and red arrows (after SAO). (b) The left column presents structural images focused on the nerve fiber layer at a ~750 μm FOV (top) and ~230 μm FOV (bottom). The right column presents the structural image in magenta overlaid by the fluorescence image in green. The fluorescence image was composited from two different focal planes for the axon and the dendrites of the RGC. Scale bars: 50 μm.

We performed fluorescein angiography to demonstrate the confocal capability to discriminate different layers in the inner retina. Figure 9 presents SAO images of three distinct vascular layers, including the NFL, IPL and OPL. The images were composited using a MIP, with the NFL in red, IPL in green, and OPL in blue to show the vessel connections in the axial direction.
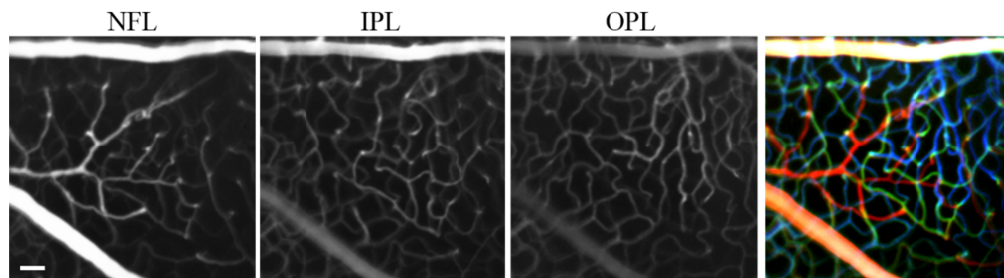

Fig. 9. Confocal SLO fluorescein angiography of a mouse retinal vasculature after Sensorless Adaptive Optics. Images (left to right) of the nerve fiber layer (NFL), inner plexiform layer (IPL), outer plexiform layer (OPL), and the MIP with the NFL in red, IPL in green, and NFL in blue. Scale bar: 50 μm.

To demonstrate the volumetric imaging ability of the system, we imaged a mouse with EGFP labeled microglia, which are located in many retinal layers. SLO images were acquired at 18 different focal positions between the OPL and NFL layer, and the axial location of the fluorescence was determined by the structural images. The depth fly-through of the back-

scattered SLO images with the co-localized fluorescence SLO image is presented in Visualization 1. Figure 10 presents images from the sequence, where the two right-most images are the structural and fluorescence images from the NFL layer. The fluorescence image in the middle-left (Fig. 10) was located immediately below the NFL layer and the image on the far-right was located deeper into the retina at the OPL. The images were color-coded in depth from the OPL to the NFL and presented with 3D shadowing that was rendered by ImageJ in Visualization 2.
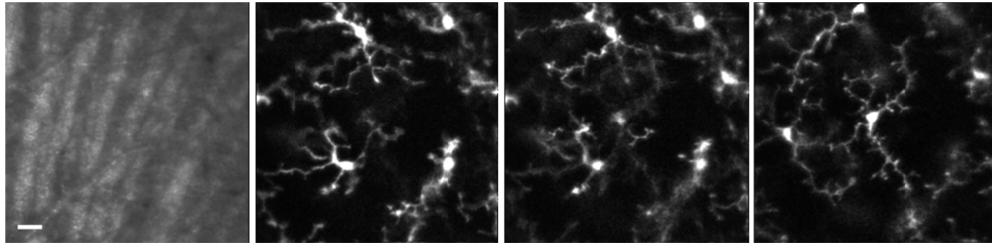

Fig. 10. Confocal SLO images with Sensorless Adaptive Optics of EGFP labeled microglia in the mouse retina (B6.129P-Cx3cr1tm1Litt/J) acquired at different focal position between the outer plexiform layer (OPL) and the nerve fiber layer (NFL) selected from Visualization 1. The microglia images were color-coded in depth between the OPL and the NFL of the retina and rendered in 3D for Visualization 2. Scale bar: 20 μm.

Microglia are known to be highly motile cells and time-lapse imaging can reveal the dynamics of the cellular branches monitoring the environment [2,32]. The microglia in Fig. 11(a) were located just below the NFL and these images were selected from a 1-hour time-lapse video that acquired images in 20 second intervals. The SAO was performed periodically throughout the imaging to ensure optimal image quality. For each optimization, the FOV was reduced to 52 μm across, containing only the microglia branches. The image in Fig. 11(b) was annotated and color-coded at these time points to highlight areas of growth and retraction. Visualization 3 presents the entire time-lapse with the time stamp of acquisition.
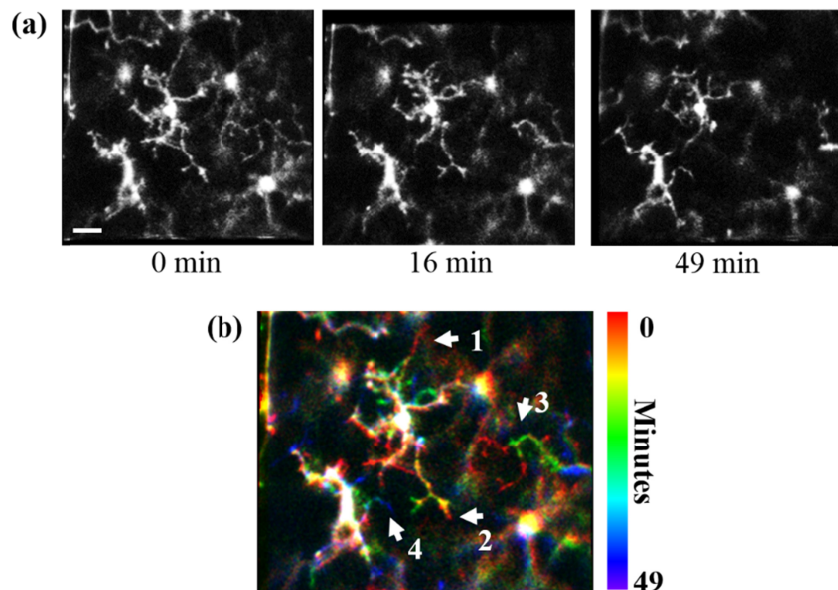

Fig. 11. (a) Confocal SLO fluorescence images with Sensorless Adaptive Optics of EGFP labeled microglia in the mouse retina (B6.129P-Cx3cr1{tm1Litt}/J) from three time points in the time-lapse video from Visualization 3. (b) The microglia images color-coded with time. The white arrows 1-4 note areas of significant growth and retraction. Scale bar: 20 μm.

The central microglia in Fig. 11(b) had a branch (white arrow #1) that retracted 24 µm, with an average velocity of 4.8 µm/min from minute 3 to minute 8, and a branch (white arrow #2) that retracted 38 µm, with an average velocity of 1.3 µm/min during minute 19 to minute 49. The microglia branch on the right of the image (white arrow #3) generally retracted over 50 minutes but also had periods of extension during that period. The microglia branch on the left (white arrow #4) appears to move towards another microglia branch (white arrow #2) at minute 24.

We performed further time-lapse imaging of microglia using the same methods for SAO in order to investigate the potential effect of the imaging light. The 488 nm imaging light was reduced to 100 µW for 39 minutes, then the exposure was increased to 230 µW and imaging proceeded for another 50 minutes, as shown in Visualization 4. Figure 12(a) shows time-points before and after the laser power was increased. The image in Fig. 12(b) was annotated and color-coded image at these time points to highlight areas of growth and retraction.
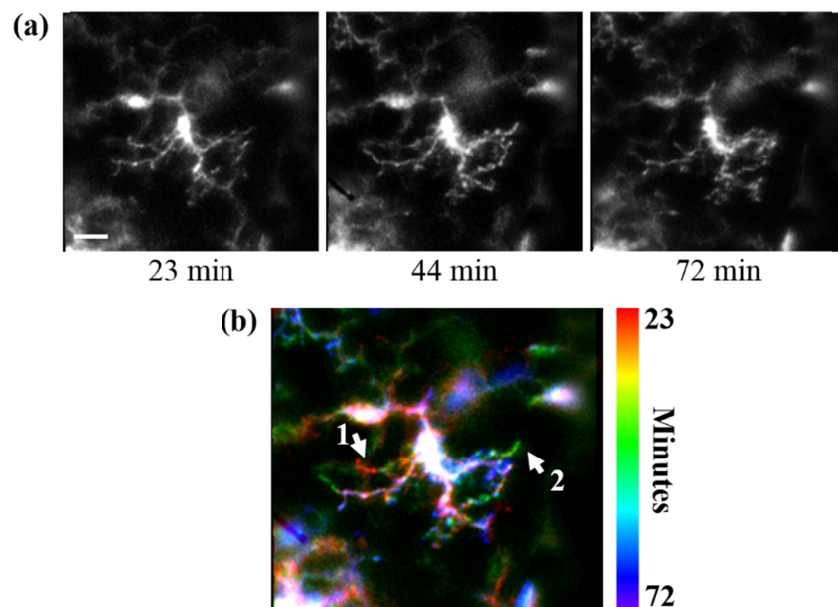

Fig. 12. (a) Confocal SLO fluorescence images with Sensorless Adaptive Optics of EGFP labelled microglia in the mouse retina (B6.129P-Cx3cr1{tm1Litt}/J) from three time points in the time-lapse video from Visualization 4 with an increase in laser power at 39 minutes. (b) The microglia images color-coded with time. The white arrows 1-2 note areas of significant growth and retraction. Scale bar: 20 µm.

4. Discussion

In this report, we have demonstrated a multi-modal *en face* imaging system with diverse functionality for vision scientists needing a variety of imaging requirements. The system imaging modalities include *en face* OCT, OCT-A, SAO OCT, as well as SLO and SAO SLO with fluorescence detection. Our system uses lens-based optical relays between the active elements, which include the VFL, the DM, and the GMs. Our results demonstrate state-of-the-art AO imaging for the mouse retina and represent improvement from our previous reported systems for each individual each modality. Our results demonstrated the variety of *in vivo* imaging abilities that included structural imaging, angiography, volumetric and time-lapse imaging of microglia cells.

The imaging system primarily used an NA of 0.25 into the mouse eye, which only represents about half of the theoretical maximum. However, with 488 nm light, this still has a calculated resolution of ~1 µm. For the purpose of this report, the image quality was

sufficient for clearly imaging the microglia branches and to report metrics, such as movement speeds, yet maintains good quality imaging without requiring AO for imaging large features. The system was initially designed and tested for mouse imaging; however, it is also capable of imaging the rat retina as well, which is often required by many vision researchers for longitudinal studies [33]. Since the rat eye is larger than the mouse eye, this decreases the maximum attainable resolution. However, it was still beneficial to have the SAO to correct for aberrations.

During the time-lapse imaging of microglia cells, we only illuminated the retina with 488 nm since we did not require the use of a beacon for WFS measurements. The microglia time-lapse in Fig. 11 appears to have more retraction than the microglia time-lapse from Fig. 12, despite the increase in laser intensity. It is possible that this was normal microglia surveillance of a healthy retina or a response to the 488 nm imaging light. If the 488 nm imaging light itself has an effect on microglia, then it may be difficult to conclude the reason for a microglia response when investigating their role in immunity studies. There is no established maximum permissible exposure (MPE) for the mouse eyes; however, other groups have scaled the MPE for SLO in human eyes [5,29,34]. The MPE for human SLO imaging decreases with imaging FOV [35], so as we image small features in small animal experiments, it will be important to continue to consider laser irradiance as a potential factor.

The imaging system was designed to be used by a non-specialist and future improvements could improve the reliability and robustness of the SAO. For example, a Region of Interest (ROI) within the display could be selected by the user instead of reducing the entire imaging FOV, which further increases the exposure during the ~10 to 20 seconds required for the optimization iteration. Real-time image tracking on the ROI would also enable the optimization algorithm to follow an object of interest or reject frames with a large amount of motion artifact [36–38]. In this work, we were using a multi-iteration exhaustive search, which was robust to the occasional motion artifact over the ~30 to 60 seconds required for the entire optimization. However, accurate image tracking would encourage the use of faster optimization algorithms, such as model-based approaches [39,40] that require much fewer measurements, thereby decreasing optimization time. This would be advantageous to further reduce the exposure of the entire imaging process and the potential for damage over time.

In this work, we optimized up to the 21st Zernike mode for 18 modes in total. The improvement in the image quality after each mode is optimized is represented in Fig. 7(b), which demonstrates that there is an increase in the metric value in the 5th radial order in the first and second iteration. Using higher orders in the optimization algorithm could improve results but it would come at the cost of algorithm time. Since time is limited for *in vivo* imaging, the algorithmic execution time is better spent on further iterations [41]. For example, the step sizes between coefficients can be reduced to improve the wavefront correction. Furthermore, successive iterations have an improved SNR, which will also improve the performance of the AO correction.

In conclusion, we have demonstrated a lens-based system, capable of high-resolution *en face* small animal imaging with multiple modalities. The compactness and simplicity of the system allow for the potential translation to vision scientists that require tools for *in vivo* and longitudinal studies. Our results demonstrate the potential for studying individual cells, such as RGCs and microglia, in healthy and diseased animal models.

Funding

Disclosures

YJ: Seymour Vision (I), MVS: Seymour Vision (I).

References

1. S. Marcos, J. S. Werner, S. A. Burns, W. H. Merigan, P. Artal, D. A. Atchison, K. M. Hampson, R. Legras, L. Lundstrom, G. Yoon, J. Carroll, S. S. Choi, N. Doble, A. M. Dubis, A. Dubra, A. Elsner, R. Jonnal, D. T. Miller, M. Paques, H. E. Smithson, L. K. Young, Y. Zhang, M. Campbell, J. Hunter, A. Metha, G. Palczewska, J. Schallek, and L. C. Sincich, "Vision science and adaptive optics, the state of the field," Vision Res. **132**, 3–33 (2017).
2. J. B. Schallek and A. Joseph, "Time-lapse imaging of retinal microglia in vivo show dynamic process motility at rest," Invest. Ophthalmol. Vis. Sci. **58**(8), 316 (2017).
3. C. Alt, J. M. Runnels, L. J. Mortensen, W. Zaher, and C. P. Lin, "In vivo imaging of microglia turnover in the mouse retina after ionizing radiation and dexamethasone treatment," Invest. Ophthalmol. Vis. Sci. **55**(8), 5314–5319 (2014).
4. Y. Geng, L. A. Schery, R. Sharma, A. Dubra, K. Ahmad, R. T. Libby, and D. R. Williams, "Optical properties of the mouse eye," Biomed. Opt. Express **2**(4), 717–738 (2011).
5. Y. Geng, A. Dubra, L. Yin, W. H. Merigan, R. Sharma, R. T. Libby, and D. R. Williams, "Adaptive optics retinal imaging in the living mouse eye," Biomed. Opt. Express **3**(4), 715–734 (2012).
6. M. Pircher and R. J. Zawadzki, "Review of adaptive optics OCT (AO-OCT): principles and applications for retinal imaging [Invited]," Biomed. Opt. Express **8**(5), 2536–2562 (2017).
7. D. R. Williams, "Imaging single cells in the living retina," Vision Res. **51**(13), 1379–1396 (2011).
8. A. Roorda, "Adaptive optics for studying visual function: a comprehensive review," J. Vis. **11**(5), 6 (2011).
9. R. Tyson, *Principles of Adaptive Optics* (CRC Press, 2010).
10. J. A. Kubby, *Adaptive Optics for Biological Imaging* (CRC Press, 2013).
11. D. P. Biss, D. Sumorok, S. A. Burns, R. H. Webb, Y. Zhou, T. G. Bifano, D. Côté, I. Veilleux, P. Zamiri, and C. P. Lin, "In vivo fluorescent imaging of the mouse retina using adaptive optics," Opt. Lett. **32**(6), 659–661 (2007).
12. R. J. Zawadzki, P. Zhang, A. Zam, E. B. Miller, M. Goswami, X. Wang, R. S. Jonnal, S. H. Lee, D. Y. Kim, J. G. Flannery, J. S. Werner, M. E. Burns, and E. N. Pugh, Jr., "Adaptive-optics SLO imaging combined with widefield OCT and SLO enables precise 3D localization of fluorescent cells in the mouse retina," Biomed. Opt. Express **6**(6), 2191–2210 (2015).
13. D. J. Wahl, C. Huang, S. Bonora, Y. Jian, and M. V. Sarunic, "Pupil segmentation adaptive optics for invivo mouse retinal fluorescence imaging," Opt. Lett. **42**(7), 1365–1368 (2017).
14. M. J. Booth, "Adaptive optical microscopy: the ongoing quest for a perfect image," Light Sci. Appl. **3**(4), e165 (2014).
15. Y. Jian, J. Xu, M. A. Gradowski, S. Bonora, R. J. Zawadzki, and M. V. Sarunic, "Wavefront sensorless adaptive optics optical coherence tomography for in vivo retinal imaging in mice," Biomed. Opt. Express **5**(2), 547–559 (2014).
16. D. J. Wahl, Y. Jian, S. Bonora, R. J. Zawadzki, and M. V. Sarunic, "Wavefront sensorless adaptive optics fluorescence biomicroscope for in vivo retinal imaging in mice," Biomed. Opt. Express **7**(1), 1–12 (2015).
17. J. Xu, K. Wong, Y. Jian, and M. V. Sarunic, "Real-time acquisition and display of flow contrast using speckle variance optical coherence tomography in a graphics processing unit," J. Biomed. Opt. **19**(2), 026001 (2014).
18. J. Xu, S. Han, C. Balaratnasingam, Z. Mammo, K. S. K. Wong, S. Lee, M. Cua, M. Young, A. Kirker, D. Albiani, F. Forooghian, P. Mackenzie, A. Merkur, D.-Y. Yu, and M. V. Sarunic, "Retinal angiography with real-time speckle variance optical coherence tomography," Br. J. Ophthalmol. **99**(10), 1315–1319 (2015).
19. A. Negrean and H. D. Mansvelder, "Optimal lens design and use in laser-scanning microscopy," Biomed. Opt. Express **5**(5), 1588–1609 (2014).
20. A. Nagler, "Plossl type eyepiece for use in astronomical instruments," U.S. patent 4482217 (February 18, 1983).
21. F. Felberer, J. S. Kroisamer, C. K. Hitzenberger, and M. Pircher, "Lens based adaptive optics scanning laser ophthalmoscope," Opt. Express **20**(16), 17297–17310 (2012).
22. Y. Jian, K. Wong, and M. V. Sarunic, "Graphics processing unit accelerated optical coherence tomography processing at megahertz axial scan rate and high resolution video rate volumetric rendering," J. Biomed. Opt. **18**(2), 026002 (2013).
23. H. R. G. W. Verstraete, M. Heisler, M. J. Ju, D. Wahl, L. Bliek, J. Kalkman, S. Bonora, Y. Jian, M. Verhaegen, and M. V. Sarunic, "Wavefront sensorless adaptive optics OCT with the DONE algorithm for *in vivo* human retinal imaging [Invited]," Biomed. Opt. Express **8**(4), 2261–2275 (2017).
24. R. A. Muller and A. Buffington, "Real-time correction of atmospherically degraded telescope images through image sharpening," J. Opt. Soc. Am. **64**(9), 1200–1210 (1974).
25. D. Debarre, M. J. Booth, and T. Wilson, "Image based adaptive optics through optimisation of low spatial frequencies," Opt. Express **15**(13), 8176–8190 (2007).
26. L. N. Thibos, R. A. Applegate, J. T. Schwiegerling, and R. Webb; VSIA Standards Taskforce Members. Vision science and its applications, "Standards for reporting the optical aberrations of eyes," J. Refract. Surg. **18**(5), S652–S660 (2002).
27. P. Zhang, J. Mocci, D. J. Wahl, R. K. Meleppat, S. K. Manna, M. Quintavalla, R. Muradore, M. V. Sarunic, S.

Bonora, E. N. Pugh, Jr., and R. J. Zawadzki, "Effect of a contact lens on mouse retinal in vivo imaging: Effective focal length changes and monochromatic aberrations," Exp. Eye Res. **172**, 86–93 (2018).

28. A. Dubra and Z. Harvey, "Registration of 2D Images from Fast Scanning Ophthalmic Instruments," in *Biomedical Image Registration*, Vol. 6204 of Lecture Notes in Computer Science (Springer, 2010), pp. 60–71.

29. N. S. Alexander, G. Palczewska, P. Stremplewski, M. Wojtkowski, T. S. Kern, and K. Palczewski, "Image registration and averaging of low laser power two-photon fluorescence images of mouse retina," Biomed. Opt. Express **7**(7), 2671–2691 (2016).

30. A. Myronenko and X. Song, "Intensity-based image registration by minimizing residual complexity," IEEE Trans. Med. Imaging **29**(11), 1882–1891 (2010).

31. M. Cua, D. J. Wahl, Y. Zhao, S. Lee, S. Bonora, R. J. Zawadzki, Y. Jian, and M. V. Sarunic, "Coherence-Gated Sensorless Adaptive Optics Multiphoton Retinal Imaging," Sci. Rep. **6**(1), 32223 (2016).

32. A. Nimmerjahn, F. Kirchhoff, and F. Helmchen, "Resting microglial cells are highly dynamic surveillants of brain parenchyma in vivo," Science **308**(5726), 1314–1318 (2005).

33. M. V. Sarunic, A. Yazdanpanah, E. Gibson, J. Xu, Y. Bai, S. Lee, H. U. Saragovi, and M. F. Beg, "Longitudinal study of retinal degeneration in a rat using spectral domain optical coherence tomography," Opt. Express **18**(22), 23435–23441 (2010).

34. L. Yin, Y. Geng, F. Osakada, R. Sharma, A. H. Cetin, E. M. Callaway, D. R. Williams, and W. H. Merigan, "Imaging light responses of retinal ganglion cells in the living mouse eye," J. Neurophysiol. **109**(9), 2415–2421 (2013).

35. F. C. Delori, R. H. Webb, and D. H. Sliney; American National Standards Institute, "Maximum permissible exposures for ocular safety (ANSI 2000), with emphasis on ophthalmic devices," J. Opt. Soc. Am. A **24**(5), 1250–1265 (2007).

36. X. Zhou, P. Bedggood, B. Bui, C. T. O. Nguyen, Z. He, and A. Metha, "Contrast-based sensorless adaptive optics for retinal imaging," Biomed. Opt. Express **6**(9), 3577–3595 (2015).

37. C. K. Sheehy, Q. Yang, D. W. Arathorn, P. Tiruveedhula, J. F. de Boer, and A. Roorda, "High-speed, image-based eye tracking with a scanning laser ophthalmoscope," Biomed. Opt. Express **3**(10), 2611–2622 (2012).

38. D. W. Arathorn, Q. Yang, C. R. Vogel, Y. Zhang, P. Tiruveedhula, and A. Roorda, "Retinally stabilized cone-targeted stimulus delivery," Opt. Express **15**(21), 13731–13744 (2007).

39. H. R. G. W. Verstraete, S. Wahls, J. Kalkman, and M. Verhaegen, "Model-based sensor-less wavefront aberration correction in optical coherence tomography," Opt. Lett. **40**(24), 5722–5725 (2015).

40. M. Booth, "Wave front sensor-less adaptive optics: a model-based approach using sphere packings," Opt. Express **14**(4), 1339–1352 (2006).

41. D. J. Wahl, P. Zhang, Y. Jian, S. Bonora, R. J. Zawadzki, and M. V. Sarunic, "Image-based adaptive optics compared to wavefront sensing methods for retinal imaging," Proc. SPIE **10502**, 105020G (2018).